agriculture

Article

Multi-Scenario Variable-State Robust Fusion Algorithm for Ranging Analysis Framework

Kaiting Xie [1], Zhaoguo Zhang [1,2,*] and Faan Wang [2]

[1] The Faculty of Mechanical and Electrical Engineering, Kunming University of Science and Technology, Kunming 650500, China; xkt@stu.kust.edu.cn
[2] The Faculty of Modern Agricultural Engineering, Kunming University of Science and Technology, Kunming 650500, China; wfa@kust.edu.cn
* Correspondence: zzg@kust.edu.cn

Abstract: Integrating modern information technology with traditional agriculture has made agricultural machinery navigation essential in PA (precision agriculture). However, agricultural equipment faces challenges such as low positioning accuracy and poor algorithm adaptability due to the complex farmland environment and various operational requirements. In this research, we proposed a generalized ranging theoretical framework with multi-scenario variable-state fusion to improve the GNSS (Global Navigation Satellite System) observation exchange performance among agricultural vehicles, and accurately measure IVRs (inter-vehicular ranges). We evaluated the effectiveness of three types of GNSS observations, including PPP-SD (precise single point positioning using single difference), PPP-TCAR (precise single point positioning using double difference based on three-carrier ambiguity resolution), and PPP-LAMBDA (precise single point positioning using double difference based on least-squares ambiguity decorrelation adjustment). Moreover, we compared the accuracy of IVRs measurements. Our framework was validated through field experiments in different scenarios. It provides insights into the appropriate use of different positioning algorithms based on the application scenario, application objects, and motion states.

Keywords: precision agriculture; GNSS; theoretical framework; precise single point positioning; inter-vehicular ranges

Citation: Xie, K.; Zhang, Z.; Wang, F. Multi-Scenario Variable-State Robust Fusion Algorithm for Ranging Analysis Framework. *Agriculture* **2024**, *14*, 516. https://doi.org/10.3390/agriculture14040516

Academic Editors: Cheng Shen, Zhong Tang and Maohua Xiao

Received: 27 February 2024
Revised: 20 March 2024
Accepted: 21 March 2024
Published: 23 March 2024

1. Introduction

The diverse and indispensable applications of the GNSS have made significant contributions to the cross-industry development and operation of modern society [1–3]. It offers precise positioning and navigation services for air, sea, land transportation, and military operations. With the integration of modern information and traditional agriculture, the GNSS has become the most critical technology for PA [4–6]. However, the sensitivity of the GNSS signals to obstacles like buildings, trees, and mountains results in low accuracy. Furthermore, adverse weather conditions and solar activity can interfere with the GNSS signals, leading to inaccurate positioning or signal disruptions. These constraints restrict the reliability and accuracy of the GNSS in agricultural sciences [7–9]. To address these challenges, further research is necessary, including the development of enhanced positioning algorithms, improved receiver design, and the implementation of assisted positioning technologies to enhance accuracy and reliability [10–12].

Therefore, scholars have made significant efforts to address the aforementioned issues. Firstly, to enhance the accuracy and reliability of the positioning system, scholars have integrated GNSS information with other sensors to compensate for the limitations of the GNSS signals when they are obstructed or interfered with. This fusion approach enables the ability of more precise and stable position information while enhancing adaptability to dynamic environments [13–15]. Taking into account the propagation delay of GNSS signals, Rohani et al. [13] proposed a Bayesian method for multi-vehicle collaborative positioning based on GNSS data and inter-vehicle distance measurements. By integrating GNSS information with information TOAs (time-of-arrivals), this method was successfully applied in workshop collaborative positioning, effectively reducing positioning uncertainty. To further improve positioning accuracy, Naseri and Koivunen et al. [14] introduced a hybrid positioning algorithm based on message passing that considers the azimuth of information transmission and integrates GNSS information with TOAs and DOA (directions-of-arrival). The enhanced algorithm was employed in vehicle distance measurements, realizing a 50% reduction in positioning error in simulation scenarios. However, in non-land scenarios like navigation, measurement information tends to be inaccurate due to the wave shadow effect. Consequently, Wu et al. [15] proposed a cooperative positioning algorithm based on an enhanced particle filter that integrates RSSI (received signal strength indicator) and GNSS information. This algorithm aims to mitigate the measurement error caused by the wave shadow effect in the observation model. Meanwhile, manufacturers are actively working on receiver design improvements to enhance the GNSS receiver sensitivity and anti-interference capabilities. Nevertheless, the wide-spread application of these technologies is limited due to the higher costs associated with multi-sensor fusion technology and equipment replacement in agriculture sciences [16–18].

Based on these considerations, numerous scholars have conducted technical research to enhance positioning algorithms and improve the accuracy of the positioning system. They have achieved this by developing new signal processing methods, optimizing satellite orbit prediction models, and refining clock calibration algorithms [19,20]. Previous studies [21–23] have focused on the pseudo-range positioning algorithm. However, the accuracy of pseudo-range positioning is limited to approximately 1 m [24], whereas precision single-point positioning based on carrier-phase measurement can achieve milli-meter-level accuracy [25]. Consequently, research attention has shifted towards carrier-phase measurement [26–28]. Lee et al. [29] explored the integration of wireless communication and Internet technology with the GNSS. By using data from additional reference stations or reference stations, they corrected errors in the GNSS signal, and then introduced a channel check statistical algorithm based on the continuous time-double difference sequence of carrier-phase measurement provided by the GNSS. The effectiveness of the proposed detection statistics was verified through experiments conducted in a multipath environment. Building upon this work, Scataglini et al. [30] proposed an aircraft attitude estimation system that utilizes a single-difference carrier phase, demonstrating higher accuracy in attitude estimation compared to a double-difference carrier phase. Simultaneously, Bai et al. [31] introduced an enhanced GNSS positioning method that leverages the time correlation between the continuous epoch code and carrier-phase measurements, thereby significantly enhancing outlier measurement robustness. Experimental results conducted using a vehicle-mounted GNSS receiver in a typical urban canyon in Hong Kong demonstrated average positioning errors of 1.76 m, but the error was reduced by 40%. To investigate the impact of the target motion state on positioning accuracy, Pin et al. [32] compared different modes of differential corrections through special experiments through static and dynamic test conditions in open agricultural sites. Such analysis confirmed that double difference clearly provides the best performance.

However, these studies were conducted for specific scenarios with stable motion conditions, and their positioning algorithm demonstrated strong matching capabilities with their application scene and the object’s motion state. Due to the complexity of the agricultural operating environment, a single technique may prove challenging to apply across different operating scenarios [33,34]. Moreover, various sources of error simultaneously affect the GNSS carrier measurement. Traditional methods of differencing the measurements to reduce correlation error can increase irrelevant error and receiver noise. Additionally, farmers and ranchers are concerned about equipment costs and seek reliable positioning solutions at a lower expense. Therefore, to exploit the full potential of precision single-point positioning algorithms in the agricultural sector, it is necessary to provide suitable positioning algorithms catering to different agricultural equipment operations to achieve an accurate location.

The main contributions of the current work are as follows.

First, to make positioning algorithms adaptive to different operating environments and motion states, we established a scenario and state-matching mechanism according to several common operation scenarios of agricultural machinery. We constructed a general theoretical framework of the multi-scenario variable-state ranging.

Secondly, this paper put forward the idea of estimating IVRs through the initial carrier-phase measurement. Under the operation environment of the agricultural machinery, this work first systematically compares the performance of PPP-SD, PPP-TCAR, and PPP-LAMBDA under the constructed framework.

Finally, an experiment platform was built, and the best matching mode of the algorithm, scenario, and state was obtained through field experiments in different scenarios. The results show that the PPP-TCAR algorithm is the most effective in the dynamic open scenario, while the PPP-LAMBDA algorithm shows better robustness in other stages.

The remainder of the paper is organized as follows. Section 2 describes the materials and methods, and an analytical framework is proposed to estimate the distance between two agricultural vehicles in three different ways using the carrier-phase observation data. Section 3 describes the distance estimation results of two agricultural vehicles in different scenarios and different motion states by using three methods. Section 4 discussed how to improve the application of GNSS positioning technology in agriculture in the future. Section 5 summarizes the contributions of this work after highlighting some essential observations from this work.

2. Materials and Methods

2.1. Ranging Model

This paper established a workshop cooperative ranging framework. As shown in Figure 1, the absolute localization position of agricultural vehicles a and b are obtained by precise point positioning, and the workshop distance is calculated by exchanging the absolute position localization.

$$D = \|\overrightarrow{P}_{Va} - \overrightarrow{P}_{Vb}\| \tag{1}$$

where D is the range between vehicles a and b. The subscript V is the agricultural vehicle. The subscripts a and b are the numbers of the two vehicles. The $\overrightarrow{P}_{Va}$ and $\overrightarrow{P}_{Vb}$ are the estimated location vectors of vehicles a and b, respectively.

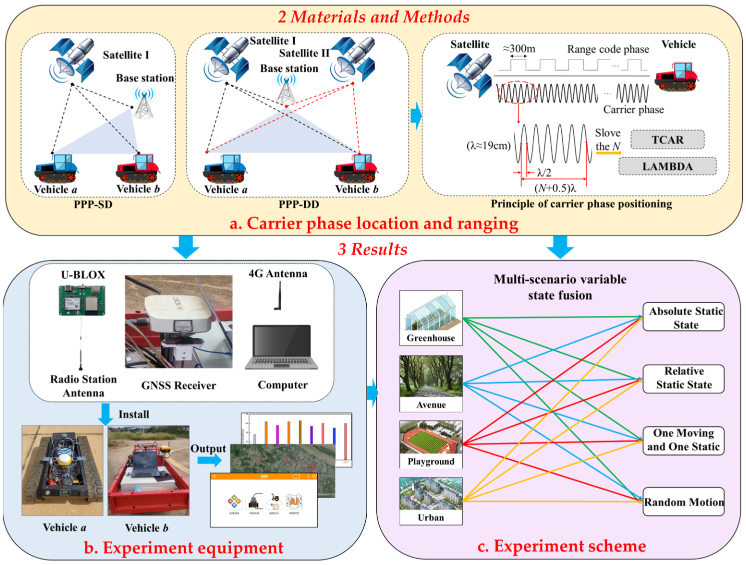

Figure 1. The framework of multi-scenario variable-state fusion ranging analysis algorithm.

2.2. Carrier Phase Location and Ranging

In this section, we described a framework that utilizes GNSS code observables to calculate the IVRs between vehicles in three different scenarios. The principle of each ranging algorithm is shown in the Figure 1a.

2.2.1. PPP-SD

PPP-SD measurements only involve the observation values of the same satellite tracked by two receivers simultaneously. In Figure 1, vehicles and base stations trace the same satellite simultaneously [20].

$$\psi_{V_a}^{(S-I)} = \lambda^{-1} \cdot (\ell_{V_a}^{(S-I)} - \Psi^{(S-I)ion} + \Psi^{(S-I)tro}) + f \cdot (\Psi_{V_a}^{(S-I)}(t) - \Psi^{(S-I)}(t)) + N_{V_a}^{(S-I)} + \zeta_{e,V_a}^{(S-I)} \tag{2}$$

$$\psi_{B}^{(S-I)} = \lambda^{-1} \cdot (\ell_{B}^{(S-I)} - \Psi^{(S-I)ion)} + \Psi^{(S-I)tro}) + f \cdot (\Psi_{B}^{(S-I)}(t) - \Psi^{(S-I)}(t)) + N_{B}^{(S-I)} + \zeta_{e,B}^{(S-I)} \tag{3}$$

$$\lambda = \frac{c}{f} \tag{4}$$

$$\psi_{V_a,B}^{(S-I)} = \psi_{V_a}^{(S-I)} - \psi_{B}^{(S-I)} \tag{5}$$

where the carrier phase is observed between satellite (S) and the receivers of vehicles a in $\psi_{V_a}^{(S-I)}$; the carrier phase is observed between satellite (S) and the receivers of the base station in $\psi_{B}^{(S-I)}$; the symbol $|\cdot|$ represents the inner product operator; λ denotes the carrier wavelength; the superscript (S), *ion*, and *tro* are satellite, ionosphere, and troposphere, respectively; the number of the satellite is expressed as the symbol $\{I, II, \ldots, M\}$; subscript B is the base station; $\ell_{V_a}^{(S-I)}$ is the true geometric range between vehicle V_a and satellite $(S-I)$; $\Psi^{(S-I)ion}$ is the ionospheric delay error; $\Psi^{(S-I)tro}$ is the tropospheric delay error; f is the carrier frequency; $\Psi_{V_a}^{(S-I)}(t)$ is the receiver clock difference of vehicle V_a at time t; $\Psi^{(S-I)}(t)$ is the clock difference of satellite $(S-I)$ at time t; $N_{V_a}^{(S-I)}$ is the overall ambiguity between vehicle V_a and satellite $(S-I)$; $\ell_{B}^{(S-I)}$ is the true geometric range between the base station and satellite $(S-I)$; $\Psi_{B}^{(S-I)}(t)$ is the receiver clock difference of the base station at time t; $N_{B}^{(S-I)}$ is the overall ambiguity between the base station and satellite $(S-I)$; $\zeta_{e,V_a}^{(S-I)}$ and $\zeta_{e,B}^{(S-I)}$ are the unknown error, representing the sum of all errors not directly reflected in (2) and (3); and c is the velocity of light.

Since the satellite is far away from vehicle a and the base station, it can be assumed that the distances between these two receivers and the satellite are parallel. Furthermore, it is assumed that the base station is at the same elevation as the vehicle. Therefore, the tropospheric single differencing error and ionospheric single differencing error between two receivers are equal, and both are 0. Here, (5) is simplified as (6).

$$\psi_{V_a,B}^{(S-I)} = \lambda^{-1} \cdot \ell_{V_a,B}^{(S-I)} + f \cdot \Psi_{V_a,B}^{(S-I)}(t) + N_{V_a,B}^{(S-I)} + \zeta_{e,V_a,B}^{(S-I)} \tag{6}$$

The single difference geometric distance $\ell_{V_a,B}^{(S-I)}$ between vehicle a and the base station to the satellite $(S-I)$ is equal to the negative number of the inner product $\ell_{V_a,B}$ between vehicle a and the base station in the direction $\ell_{B}^{(S-I)}$ of the base station to the satellite $(S-I)$ observation.

$$\ell_{V_a,B}^{(S-I)} = -\ell_{V_a,B} \cdot \ell_{B}^{(S-I)} \tag{7}$$

Assume that the vehicle a and the reference station receiver jointly generate measurements for M^{th} different satellites and that the M^{th} single difference carrier-phase measurements they comprise at the exact moment are $\psi_{V_a,B}^{(S-I)}, \psi_{V_a,B}^{(S-II)}, \ldots, \psi_{V_a,B}^{(S-M)}$. Then, the corresponding M^{th} single difference carrier phase observation equations form the following matrix equation.

$$\begin{bmatrix} \psi_{V_a,B}^{(S-I)} \\ \psi_{V_a,B}^{(S-II)} \\ \vdots \\ \psi_{V_a,B}^{(S-M)} \end{bmatrix} = -\lambda^{-1} \cdot \begin{bmatrix} \ell_{V_a,B}^{(S-I)} & 1 \\ \ell_{V_a,B}^{(S-II)} & 1 \\ \vdots & \vdots \\ \ell_{V_a,B}^{(S-M)} & 1 \end{bmatrix} \begin{bmatrix} \ell_{V_a,B} \\ c \cdot \Psi_{V_a,B}^{(S-I)}(t) \end{bmatrix} + \begin{bmatrix} N_{V_a,B}^{(S-I)} \\ N_{V_a,B}^{(S-II)} \\ \vdots \\ N_{V_a,B}^{(S-M)} \end{bmatrix} \tag{8}$$

The single-difference carrier-phase measurements at the adjacent moments t_n and t_{n+1} are $\psi_{V_a,B,t_n}^{(S-I)}$ and $\psi_{V_a,B,t_{n+1}}^{(S-I)}$, respectively.

$$\begin{bmatrix} \psi_{V_a,B,t_{n+1}}^{(S-I)} \\ \psi_{V_a,B,t_{n+1}}^{(S-II)} \\ \vdots \\ \psi_{V_a,B,t_{n+1}}^{(S-M)} \end{bmatrix} - \begin{bmatrix} \psi_{V_a,B,t_n}^{(S-I)} \\ \psi_{V_a,B,t_n}^{(S-II)} \\ \vdots \\ \psi_{V_a,B,t_n}^{(S-M)} \end{bmatrix} = -\lambda^{-1} \cdot \boldsymbol{G}_{t_{n+1}} \cdot \begin{bmatrix} \ell_{V_a,B,t_{n+1}} \\ c \cdot \Psi_{V_a,B,t_{n+1}}^{(S-I)}(t) \end{bmatrix} + -\lambda^{-1} \cdot \boldsymbol{G}_{t_n} \cdot \begin{bmatrix} \ell_{V_a,B,t_n} \\ c \cdot \Psi_{V_a,B,t_n}^{(S-I)}(t) \end{bmatrix} \tag{9}$$

$$\begin{bmatrix} \Delta\ell_{V_a,B} \\ \Delta\Psi_{V_a,B}^{(S-I)}(t) \end{bmatrix} = \begin{bmatrix} \ell_{V_a,B,t_{n+1}} \\ \Psi_{V_a,B,t_{n+1}}^{(S-I)}(t) \end{bmatrix} - \begin{bmatrix} \ell_{V_a,B} \\ \Psi_{V_a,B}^{(S-I)}(t) \end{bmatrix} \tag{10}$$

$$\begin{bmatrix} \psi_{V_a,B,t_{n+1}}^{(S-I)} - \psi_{V_a,B,t_n}^{(S-I)} \\ \psi_{V_a,B,t_{n+1}}^{(S-II)} - \psi_{V_a,B,t_n}^{(S-II)} \\ \vdots \\ \psi_{V_a,B,t_{n+1}}^{(S-M)} - \psi_{V_a,B,t_n}^{(S-M)} \end{bmatrix} = -\lambda^{-1} \cdot \boldsymbol{G}_{t_{n+1}} \cdot \begin{bmatrix} \ell_{V_a,B} \\ c \cdot \Psi_{V_a,B}^{(S-I)}(t) \end{bmatrix} + \lambda^{-1} \cdot (\boldsymbol{G}_{t_{n+1}} - \boldsymbol{G}_{t_n}) \cdot \begin{bmatrix} \ell_{V_a,B,t_n} \\ c \cdot \Psi_{V_a,B,t_n}^{(S-I)}(t) \end{bmatrix} \tag{11}$$

where $\boldsymbol{G}$ is a geometric matrix; $\ell_{V_a,B}$ is a baseline vector; $\Psi_{V_a,B}^{(S-I)}(t)$ is the clock difference of the single difference receiver; $\Delta\ell_{V_a,B}$ and $\Delta\Psi_{V_a,B}^{(S-I)}(t)$ are the change in $\Delta\ell_{V_a,B}$ and $\Delta\Psi_{V_a,B}^{(S-I)}(t)$ between these two moments, respectively.

Equation (10) cancels the single-difference whole-cycle ambiguity vector forward and backward. However, the mean square error of the single difference measurement noise $\zeta_{e,V_a,B}^{(S-I)}$ increases to the $\sqrt{2}$ times of the initial carrier-phase measurement noise, which will be eliminated by the double difference.

2.2.2. PPP-DD

The double difference measurements consist of two receivers measuring the satellite at the same time [35]. As shown in Figure 1, the vehicle receiver a and the base station B track both satellites $(S-I)$ and $(S-II)$ simultaneously, while their single-difference carrier-phase measurement for satellite $(S-II)$ is $\psi_{V_a,B}^{(S-II)}$.

$$\psi_{V_a,B}^{(S-II)} = \lambda^{-1} \cdot \ell_{V_a,B}^{(S-II)} + f \cdot \Psi_{V_a,B}^{(S-II)}(t) + N_{V_a,B}^{(S-II)} + \zeta_{e,V_a,B}^{(S-II)} \tag{12}$$

The double-difference carrier-phase measurement $\psi_{V_a,B}^{(S-I,II)}$ is defined as follows.

$$\psi_{V_a,B}^{(S-I,II)} = \psi_{V_a}^{(S-I)} - \psi_{V_a,B}^{(S-II)} \tag{13}$$

By substituting (6) and (12) into (13), the observation equation of the double difference measurement value $\psi_{V_a,B}^{(S-I,II)}$ is:

$$\psi_{V_a,B}^{(S-I,II)} = \lambda^{-1} \cdot \ell_{V_a,B}^{(S-I,II)} + f \cdot \Psi_{V_a,B}^{(S-I,II)}(t) + N_{V_a,B}^{(S-I,II)} + \zeta_{e,V_a,B}^{(S-I,II)} \tag{14}$$

Equation (14) indicates that the double difference can eliminate the receiver and satellite clock difference.

$$\ell_{V_a,B}^{(S-II)} = -\ell_{V_a,B} \cdot \ell_{B}^{(S-II)} \tag{15}$$

The double difference consists of $(M-1)^{th}$ double-difference carrier-phase measurements.

$$\begin{bmatrix} \psi_{V_a,B}^{(S-I,II)} \\ \psi_{V_a,B}^{(S-I,III)} \\ \vdots \\ \psi_{V_a,B}^{(S-I,M)} \end{bmatrix} = -\lambda^{-1} \cdot \begin{bmatrix} -\left(\ell_{V_a,B}^{(S-II)} - \ell_{B}^{(S-I)}\right)^T \\ -\left(\ell_{V_a,B}^{(S-III)} - \ell_{B}^{(S-I)}\right)^T \\ \vdots \\ -\left(\ell_{V_a,B}^{(S-M)} - \ell_{B}^{(S-I)}\right)^T \end{bmatrix} \cdot \ell_{V_a,B} + \begin{bmatrix} N_{V_a,B}^{(S-I)} \\ N_{V_a,B}^{(S-II)} \\ \vdots \\ N_{V_a,B}^{(S-M)} \end{bmatrix} \tag{16}$$

The cost of the double difference is to increase the mean square error of the double-difference measurement noise $\zeta_{e,V_a,B}^{(S-I,II)}$ to $\sqrt{2}$ times the mean square error of the original single-difference measurement noise $\zeta_{e,V_a,B}^{(S-I)}$, and sacrifice an observation equation.

If the whole cycle ambiguity value of each double difference in (16) can be determined, the baseline vector $\Delta\ell_{V_a,B}$ can be solved from this equation, thus achieving relative positioning. The next section describes two different algorithms for fixing the ambiguity of the double-difference round: Three-Carrier Ambiguity Resolution (TCAR) and Least-squares Ambiguity Decorrelation Adjustment (LAMBDA).

2.2.3. PPP-TCAR

The PPP-TCAR generates a series of combined measurements with different beat frequency wavelengths by linearly combining multi-frequency measurements and then solves the whole-period ambiguity in all individual combinations step by step along the sequence from the most comprehensive aisle combination to the narrowest aisle combination [36]. The observation equation of the double-difference super-wide lane carrier-phase measurement $\psi_{\omega 23}$ is:

$$\psi_{\omega 23} = \lambda_{\omega 23}^{-1} \cdot (\ell + g + \Upsilon) - \Upsilon_{\omega 23} + N_{\omega 23} + \zeta_{\omega 23} \tag{17}$$

where $\lambda_{\omega 23}$ is the wide-lane carrier wavelength. The subscripts 1, 2, and 3 are the number of GNSS carrier frequencies of L1, L2, and L5, respectively; g is the double-difference ephemeris error. Since all the measurements discussed in this section are double difference, the original receiver subscript V, B, and satellite superscript (S) in the double-difference measurement symbols are omitted to simplify the expression. Neglecting the double-differential ionospheric delay residuals in the short baseline case, the whole-period ambiguity of the ultra-wide-alley carrier-phase measurements $N_{\omega 23}$ is:

$$N_{\omega 23} = \left[\psi_{\omega 23} - \frac{\rho_3}{\lambda_{\omega 23}} \right] \tag{18}$$

$$\hat{\zeta}_{\omega 23} = (\psi_{\omega 23} - N_{\omega 23}) \cdot \lambda_{\omega 23} = (\ell + g + \Upsilon) - \lambda_{\omega 23} \cdot \Upsilon_{\omega 23} + \zeta_{\omega 23} \tag{19}$$

where ρ_3 is the double-difference pseudo-range measurement, and $\hat{\zeta}_{\omega 23}$ is the high-precision double-difference measurement value.

The double-difference measurement $\psi_{\omega 23}$ without the whole-period ambiguity obtained from (19) is used to solve the whole-period ambiguity of the double-difference wide-aisle carrier-phase measurement $\psi_{\omega 12}$. The observation equation for the double-difference wide-aisle measurement $\psi_{\omega 12}$ is as follows.

$$\psi_{\omega 12} = \lambda_{\omega 12}^{-1} \cdot (\ell + g + \Upsilon) - \Upsilon_{\omega 12} + N_{\omega 12} + \zeta_{\omega 12} \tag{20}$$

$$N_{\omega 12} = \left[\psi_{\omega 23} - \frac{\hat{\zeta}_{\omega 23}}{\lambda_{\omega 12}} \right] \tag{21}$$

$$\hat{\zeta}_{\omega 12} = (\psi_{\omega 12} - N_{\omega 12}) \cdot \lambda_{\omega 12} = (\ell + g + \Upsilon) - \lambda_{\omega 12} \cdot \Upsilon_{\omega 12} + \zeta_{\omega 12} \tag{22}$$

Using the double-difference distance measurement without the integer ambiguity $\hat{\zeta}_{\omega 12}$ obtained from (22) to solve for the integer ambiguity in the double-difference carrier-phase measurement ψ_1, on carrier L1:

$$N_1 = [\psi_1 - \hat{\zeta}_{\omega 12}\lambda_1] \tag{23}$$

$$N_{\omega 12} = N_1 - N_2 \tag{24}$$

$$N_{\omega 23} = N_2 - N_3 \tag{25}$$

2.2.4. PPP-LAMBDA

The PPP-LAMBDA algorithm is a fast method for solving the double-difference whole-period ambiguity that can be applied to real-time dynamic and static positioning systems [37]. The relative localization equation based on the double-difference carrier phase is expressed as a linear matrix.

$$\boldsymbol{y} = \boldsymbol{A}(\Delta \boldsymbol{b}_{\boldsymbol{VB}}) + \boldsymbol{BN} \tag{26}$$

where y is the vector of double-difference carrier-phase measurements given by the receiver, and $\Delta \boldsymbol{b}_{VB}$ is the unknown baseline vector correction. $\boldsymbol{N}$ is the double-difference integer ambiguity vector to be solved, and $\boldsymbol{A}$ and $\boldsymbol{B}$ are the constant coefficient matrices.

$$\min_{\Delta \boldsymbol{b}_{VB}, N} \|\boldsymbol{y} - \boldsymbol{A}(\Delta \boldsymbol{b}_{VB}) - \boldsymbol{BN}\|_{\boldsymbol{C}}^2 = \min_{\Delta \boldsymbol{b}_{VB}, N} (\boldsymbol{y} - \boldsymbol{A}(\Delta \boldsymbol{b}_{VB}) - \boldsymbol{BN})^T C (y - A(\Delta \boldsymbol{b}_{VB}) - \boldsymbol{BN}) \tag{27}$$

where $\boldsymbol{C}$ is the weight coefficient matrix.

$$\boldsymbol{Q}_{[\Delta \hat{\boldsymbol{b}}_{VB}, \hat{\boldsymbol{N}}]} = Cov \begin{bmatrix} \Delta \hat{\boldsymbol{b}}_{VB} \\ \hat{\boldsymbol{N}} \end{bmatrix} = \begin{bmatrix} \boldsymbol{Q}_{\Delta \hat{\boldsymbol{b}}_{VB}} & \boldsymbol{Q}_{\Delta \hat{\boldsymbol{b}}_{VB}, \hat{\boldsymbol{N}}} \\ \boldsymbol{Q}^T_{\Delta \hat{\boldsymbol{b}}_{VB}, \hat{\boldsymbol{N}}} & \boldsymbol{Q}_{\hat{\boldsymbol{N}}} \end{bmatrix} \tag{28}$$

where $\boldsymbol{Q}_{[\Delta \hat{\boldsymbol{b}}_{VB}, \hat{\boldsymbol{N}}]}$ is the covariance matrix; $\Delta \hat{\boldsymbol{b}}_{VB}$ and $\hat{\boldsymbol{N}}$ are floating-point weighted least squares solutions; $\boldsymbol{Q}_{\Delta \hat{\boldsymbol{b}}_{VB}}$ is the covariance matrix of $\Delta \hat{\boldsymbol{b}}_{VB}$; $\boldsymbol{Q}_{\hat{N}}$ is the covariance matrix of $\hat{\boldsymbol{N}}$; and $\boldsymbol{Q}_{\Delta \hat{\boldsymbol{b}}_{VB}}$ represents the correlation between $\Delta \hat{\boldsymbol{b}}_{VB}$ and $\boldsymbol{Q}_{\hat{\boldsymbol{N}}}$.

Using the distance squared between the integer vector $\boldsymbol{N}$ and the floating-point solution $\hat{\boldsymbol{N}}$ as the objective function, we search for the integer perimeter ambiguity $\boldsymbol{N}$ to minimize this objective function.

$$\min_{\boldsymbol{N}} \|\boldsymbol{N} - \hat{\boldsymbol{N}}\|^2_{\boldsymbol{Q}^{-1}_{\hat{\boldsymbol{N}}}} \tag{29}$$

$$\|\boldsymbol{N} - \hat{\boldsymbol{N}}\|^2_{\boldsymbol{Q}^{-1}_{\hat{\boldsymbol{N}}}} < T \tag{30}$$

where T is a threshold that takes the appropriate value. The search space defined by (30) is a multidimensional ellipsoid, and the integral numerical grid points inside the sphere need to be searched and investigated theoretically one by one. One of the crucial numerical grid points can satisfy (29).

In order to make the optimal integer solution $\breve{\boldsymbol{N}}$ appear near the floating-point solution $\hat{\boldsymbol{N}}$, and accordingly restrict the search near $\hat{\boldsymbol{N}}$ to improve the search efficiency, the PPP-LAMBDA algorithm transforms the original search for $\boldsymbol{N}$ inside a narrow and long ellipsoid into a search for $\boldsymbol{P}$ in an approximate sphere space through the following $\boldsymbol{Z}$-transformation.

$$\boldsymbol{P} - \hat{\boldsymbol{P}} = \boldsymbol{Z}(\boldsymbol{N} - \hat{\boldsymbol{N}}) \tag{31}$$

$$\min_{\boldsymbol{N}} \|\boldsymbol{N} - \hat{\boldsymbol{N}}\|^2_{\boldsymbol{Q}^{-1}_{\hat{\boldsymbol{N}}}} = \min_{\boldsymbol{P}} \|\boldsymbol{P} - \hat{P}\|^2_{\boldsymbol{Z}^{-T}\boldsymbol{Q}^{-1}_{\hat{\boldsymbol{N}}}\boldsymbol{Z}^{-1}} \tag{32}$$

where the power factor is changed from the original $\boldsymbol{Q}_{\hat{N}}^{-1}$ to the diagonal array $\boldsymbol{Z}^{-T}\boldsymbol{Q}_{\hat{N}}^{-1}\boldsymbol{Z}^{-1}$. Its most integer solution $\breve{\boldsymbol{P}}$ is directly equal to the rounded value of the vector $\hat{\boldsymbol{P}}$.

$$\breve{\boldsymbol{N}} = \boldsymbol{Z}^{-1}\breve{\boldsymbol{P}} \tag{33}$$

3. Results

Field experiments were conducted to validate the performance and applicability of three methods utilizing carrier phase for ranging in real-world scenarios. This section provides a comprehensive description of these experiments, presents the results obtained from all methods, and thoroughly discusses these findings.

3.1. Experimental Setup

The present study utilized two agricultural tracked vehicles equipped with an AnavS sensor module (AnavS, Munich, Germany) and a U-Blox M8T receiver (ComVav Technology Ltd., Shanghai, China), configured to provide raw GNSS data at a frequency of 5 Hz. The GNSS active antennas were mounted atop each vehicle, and the raw GNSS data were collected and stored in a laptop computer within each vehicle for post-processing. The experiment equipment is shown in the Figure 1b. The propagation of satellite signals was impacted by various environmental factors, such as cover and "urban canyons", which caused a reduction in collection points and, in turn, affected the accuracy of positioning (Figure 2).

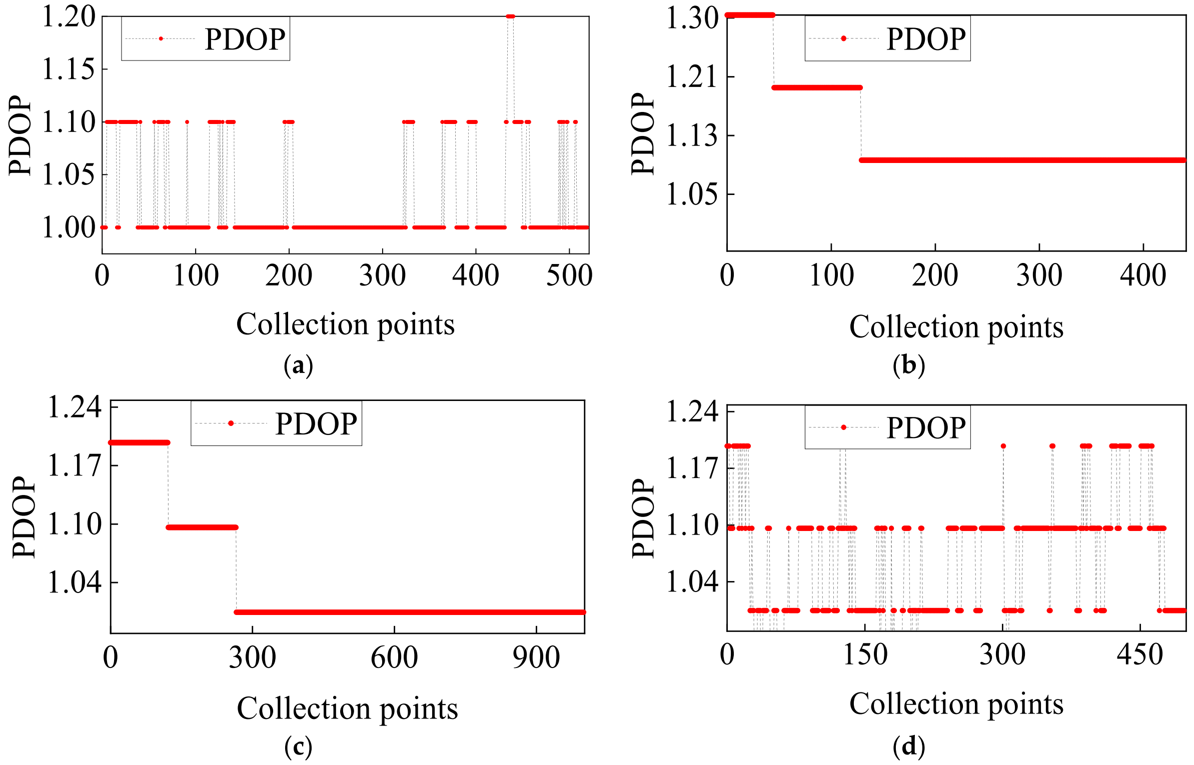

Figure 2. The PDOP of satellites in different scenarios. (**a**) Greenhouse, $\mathrm{MAX_{CP}}$ = 521; (**b**) avenue, $\mathrm{MAX_{CP}}$ = 441; (**c**) playground, $\mathrm{MAX_{CP}}$ = 1002; (**d**) urban, $\mathrm{MAX_{CP}}$ = 500.

To account for these factors, this study employed four scenarios: complete-cover greenhouse, partial-cover avenue, open playground, and urban area with multi-path effects (Figure 3).

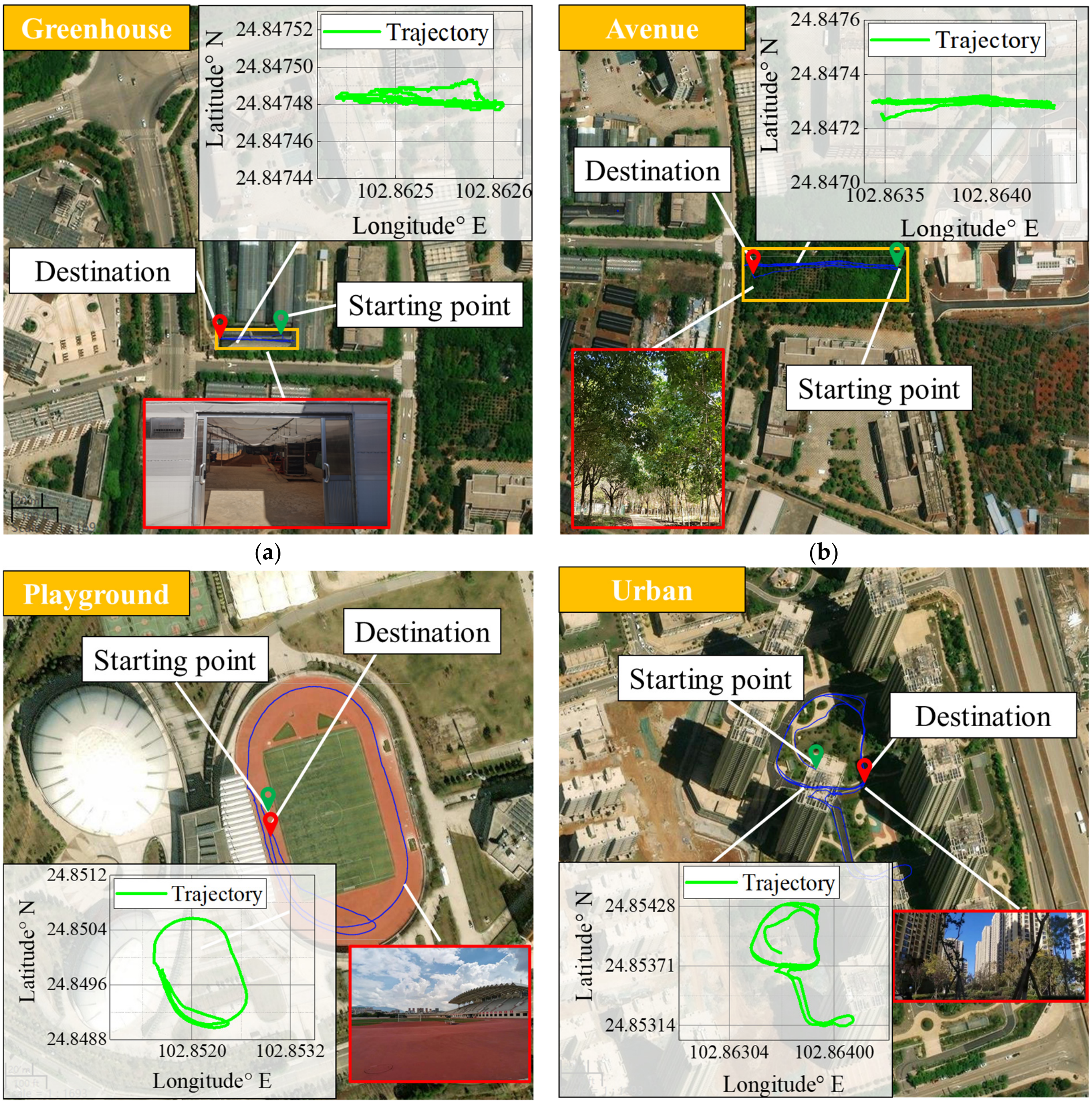

(**a**) (**b**)

(**c**) (**d**)

Figure 3. Vehicle trajectory; (**a**) greenhouse; (**b**) avenue; (**c**) playground; (**d**) urban.

As shown in the Figure 1c, the experiment involved three algorithmic methods, namely, PPP-SD, PPP-TCAR, and PPP-LAMBDA, which were validated using absolute stillness, relative stillness with a dynamic and static vehicle, and two random dynamic moving vehicles. The experimental scheme is shown in Table 1.

Table 1. Experimental scheme.

Experimental Types	True Distance of ASE/m	Sampling Time/min	Sampling Days/d	Replicated Experimental Units
ASE	(5, 50), dim = 5	15	15	10
RSE	(1, 10), dim = 1	15	15	10
OMOSE	(0, 50), dim = 5	15	15	10
RME	Random	15	15	10

3.2. ASE (Absolute Static Experiment)

The first set of experiments was conducted for absolute stationary positioning data acquisition. Two vehicles were parked stationary in different scenarios, and the positioning data of the two chassis were collected for the same timestamp (15 min) and at different distances each day. Three algorithms, PPPSD, PPP-TCAR, and PPP-LAMBDA, were used to optimize the collected data. Figures 4–7 show the deviation between the localization distance and the actual distance processed by the three algorithms, with an accurate distance of 5 cm.

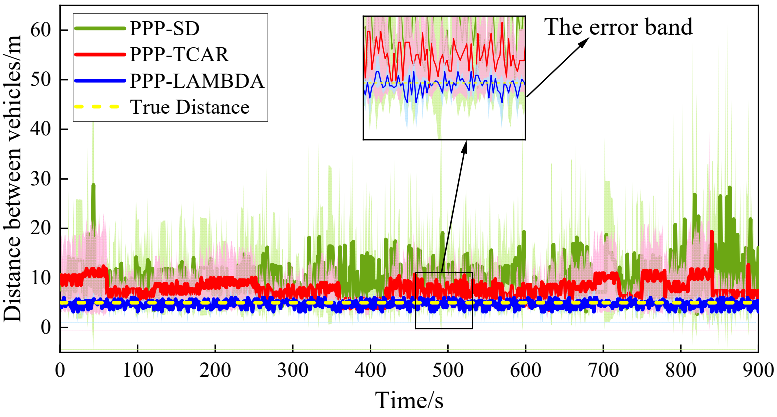

Figure 4. The distance between vehicles of ASE in greenhouse.

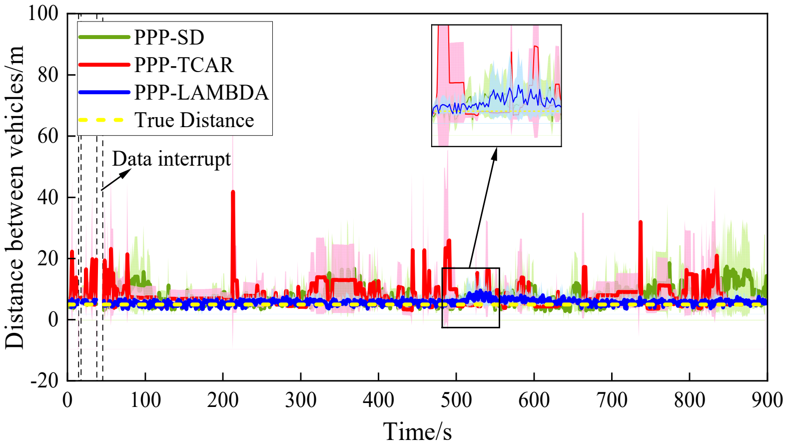

Figure 5. The distance between vehicles of ASE in avenue.

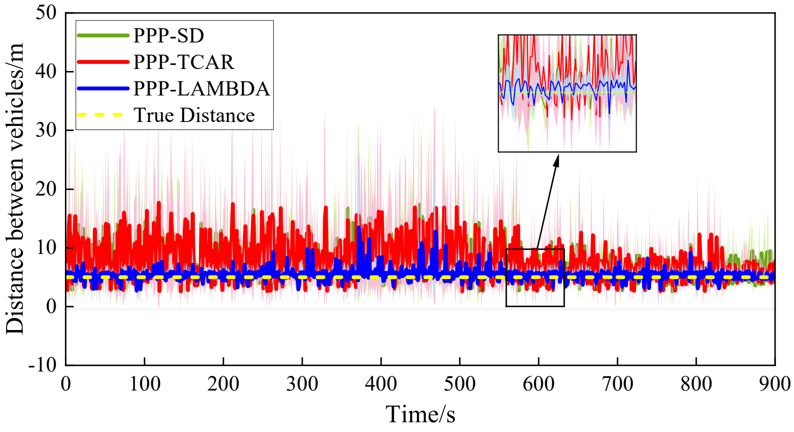

Figure 6. The distance between vehicles of ASE in playground.

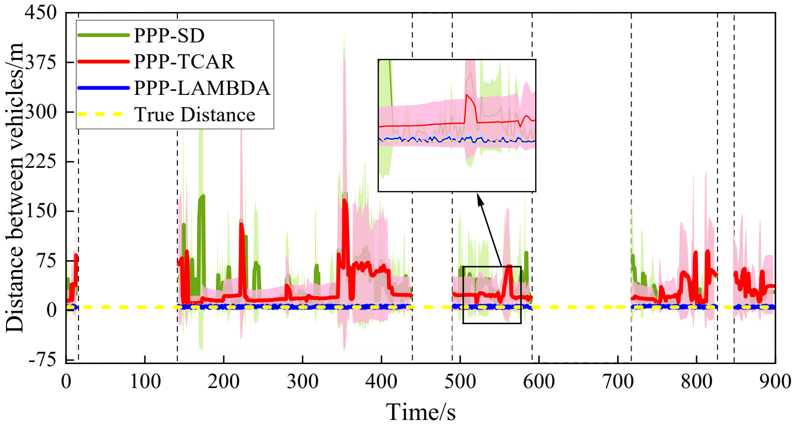

Figure 7. The distance between vehicles of ASE in urban.

Although precision single-point positioning integrates the advantages of standard single-point positioning and differential positioning, using the precision ephemeris and clock difference calculated from the data collected by the global monitoring station, the non-difference data processing of the phase and pseudo-distance measurements observed by a single receiver can reach centimetre-level positioning accuracy and is not limited by the operating distance [28]. The significant reduction in the number of satellites makes the error of the PPP-SD method relatively large. While the PPP-DD algorithm obtains accurate position information, the corresponding high-precision clock difference and tropospheric delay estimators can be obtained by solving the whole-circle ambiguity through PPP-LAMBDA. Hence, the PPP-LAMBDA algorithm has a minor error. The accuracy of the PPP-TCAR algorithm is at the intermediate level in this scenario and state, and the data are shown in Table 2. The second experiment scenario was an avenue with dense leaves. Although there was a shelter on the avenue, it was less sheltered than the shady shed, called semi-sheltered. Compared with the data processing results of the three algorithms, the accuracy of the three algorithms was slightly improved in the semi-shaded shaded shed scene, and the PPP-LAMBDA algorithm was still the best. In the open playground environment, the accuracy of the three methods is significantly improved compared with the first two environments due to the significant increase in the visible number of satellites. However, due to the "urban canyons" phenomenon in the residential area, there is a multipath effect and positioning error. When the two positioning targets are stationary, the PPP-LAMBDA algorithm maintains stable positioning accuracy in the four environments with robustness. Under full shelter, the PPP-LAMBDA algorithm has the highest accuracy.

Table 2. Average error of ASE.

Algorithm	**Average Error of ASE/%**			
	Complete-Cover Greenhouse	**Partial-Cover Avenue**	**Open Playground**	**Urban**
PPP-SD	6.73	3.95	4.64	41.06
PPP-TCAR	4.06	4.27	4.64	36.09
PPP-LMBDA	0.83	1.30	0.30	1.48

3.3. RSE (Relative Static Experiment)

The second set of tests was relatively static, in which the distance between vehicles *a* and *b* remained constant while moving vehicles *a* and *b*. The positioning data of the two vehicles were collected within 15 min (Figures 8–11). As shown in Table 3, the analysis showed that the PPP-LAMBDA algorithm had the highest accuracy in the full-shade, semi-shade, and cell scenarios. Furthermore, the PPP-TCAR algorithm had the highest accuracy in the open playground scenario. Meanwhile, the PPP-TCAR algorithm is the most accurate and less computationally intensive in open environments with moving localization targets.

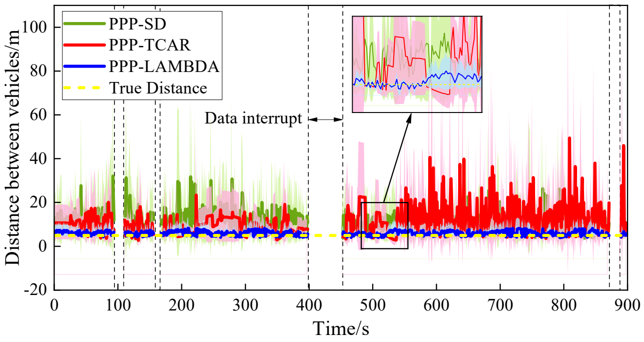

Figure 8. The distance between vehicles of RSE in greenhouse.

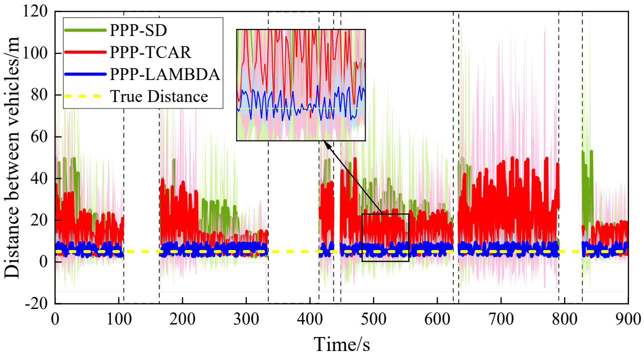

Figure 9. The distance between vehicles of RSE in avenue.

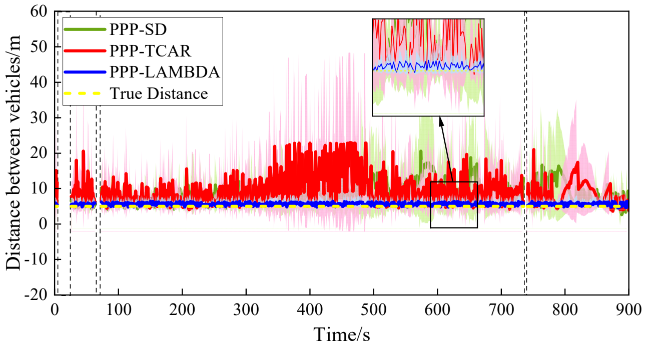

Figure 10. The distance between vehicles of RSE in playground.

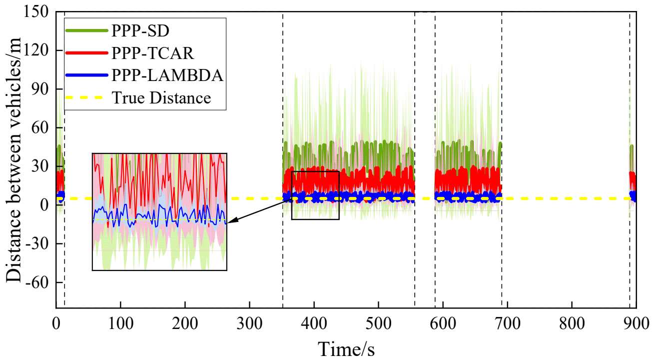

Figure 11. The distance between vehicles of RSE in urban.

Table 3. Average error of RSE.

Algorithm	**Average Error of RSE /%**			
	Complete-Cover Greenhouse	**Partial-Cover Avenue**	**Open Playground**	**Urban**
PPP-SD	8.67	17.22	5.53	32.40
PPP-TCAR	9.19	16.88	6.63	16.00
PPP-LMBDA	1.57	2.66	0.91	2.98

3.4. OMOSE (One Moving and One Stationary Experiment)

The third group is a dynamic cooperative experiment, where the position of vehicle *a* is fixed, and vehicle *b* is moved to a specified distance at different speeds at a constant rate. The positioning data of vehicle *a* and *b* were collected during the moving time. It is concluded that the PPP-LAMBDA algorithm has better robustness in complete cover, partial cover, and multipath effects when vehicle *a* is stationary and vehicle *b* is moving. In contrast, the PPP-TCAR algorithm has the highest localization accuracy in open scenarios (Figures 12–15). As shown in Figure 16, the PPP-LAMBDA error accumulation is the smallest when the vehicle is in the woods and the cell, while the PPP-TCAR error accumulation is the smallest when the vehicle is in the playground.

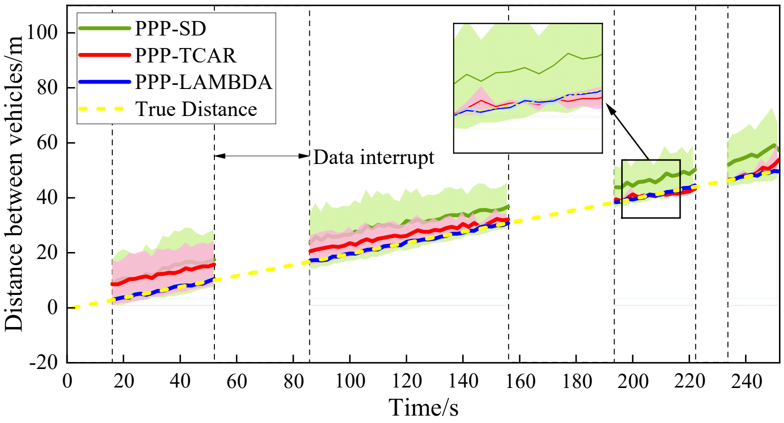

Figure 12. The distance between vehicles of OMOSE in greenhouse.

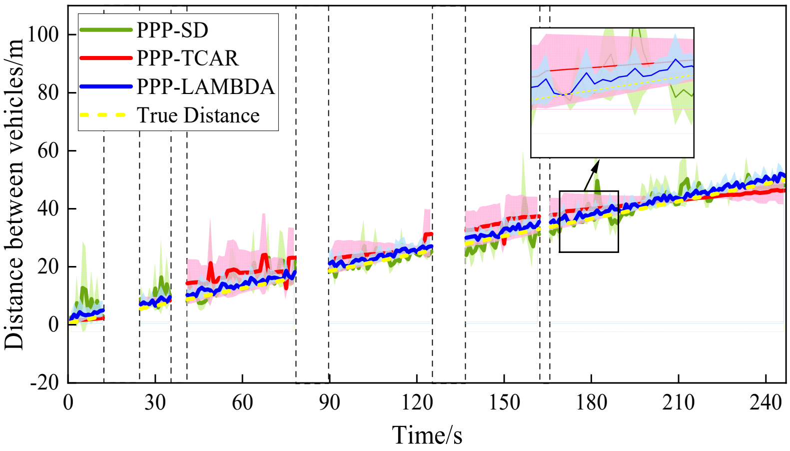

Figure 13. The distance between vehicles of OMOSE in avenue.

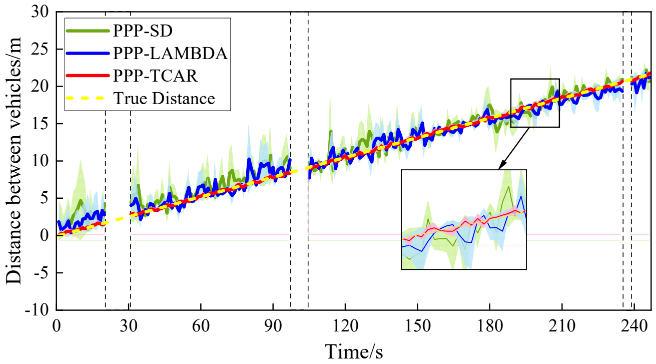

Figure 14. The distance between vehicles of OMOSE in playground.

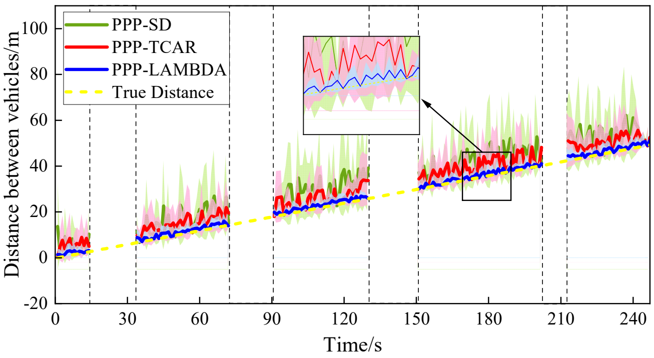

Figure 15. The distance between vehicles of OMOSE in urban.

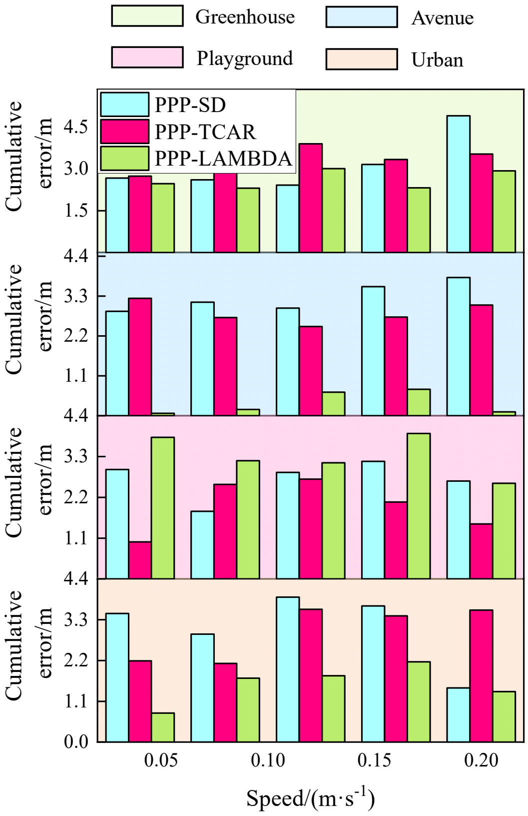

Figure 16. The cumulative error.

Figure 17 shows that the errors of the three algorithms increase with the increase in the moving distance at different moving speeds.

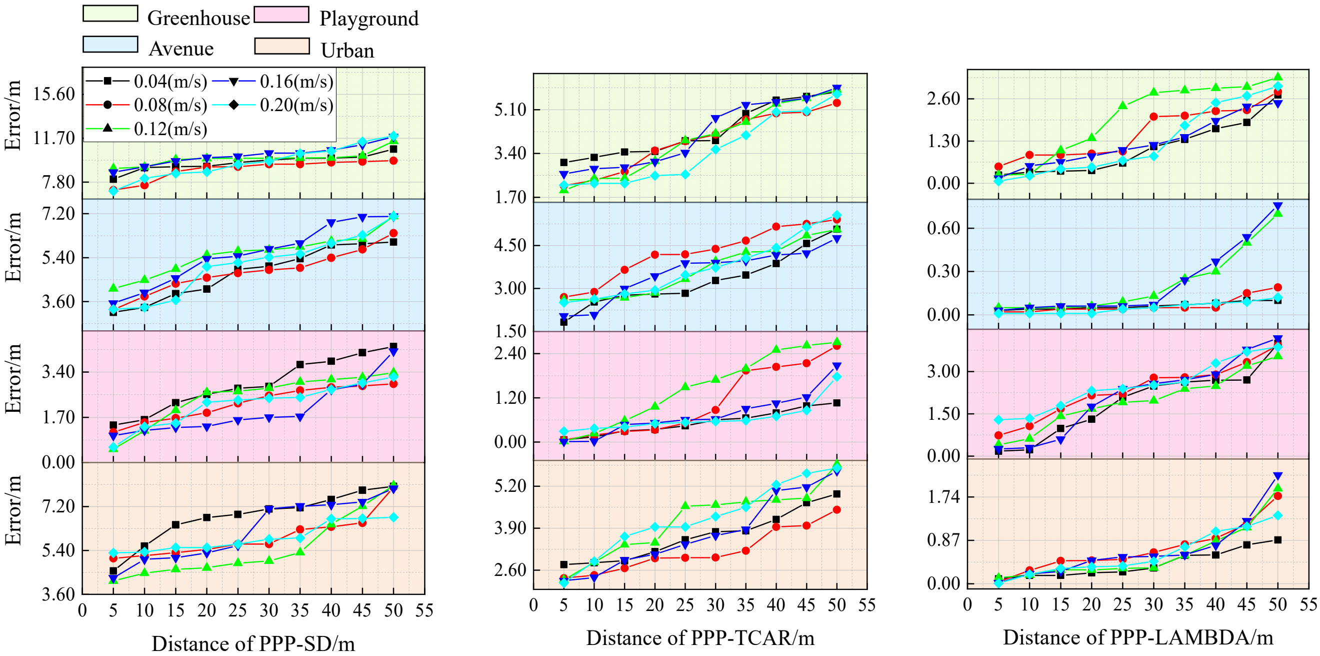

(**a**) (**b**) (**c**)

Figure 17. The error at different speeds of OMOSE; (**a**) PPP-SD; (**b**) PPP-TCAR; (**c**) PPP-LAMBDA.

The standard deviations of the three algorithms are obtained for different scenarios, moving distances, and moving speeds, and the results are shown in Table 4.

Table 4. Average error of OMOSE.

Algorithm	**Average Error of OMOSE/%**			
	Complete-Cover Greenhouse	**Partial-Cover Avenue**	**Open Playground**	**Urban**
PPP-SD	9.63	3.29	1.27	9.36
PPP-TCAR	4.18	4.23	0.18	6.41
PPP-LMBDA	0.36	2.07	0.99	1.52

3.5. RME (Random Motion Experiment)

The fourth group is a two-vehicles random dynamic cooperative experiment, where vehicles *a* and *b* move randomly in the same scene, and the positioning data of vehicles a and b were collected during the moving time. The error is shown in Table 5. Like the relative stationary trials, PPP-TCAR has higher accuracy in the open environment when both positioning targets are moving (Figures 18–21).

Table 5. Average error of RME.

Algorithm	**Average Error of RME/%**			
	Complete-Cover Greenhouse	**Partial-Cover Avenue**	**Open Playground**	**Urban**
PPP-SD	4.34	5.16	2.36	6.07
PPP-TCAR	3.96	3.70	0.90	3.79
PPP-LMBDA	1.43	0.12	2.18	0.60

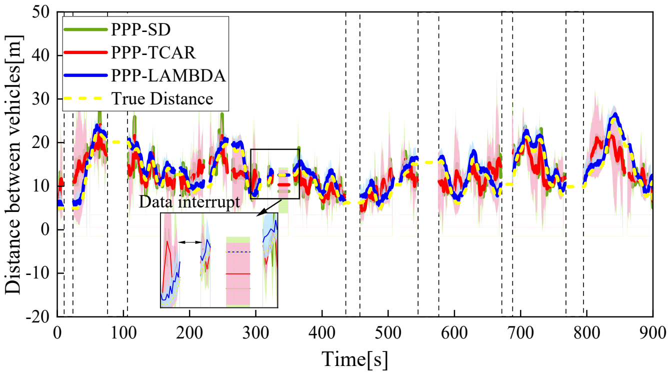

Figure 18. The distance between vehicles of RME in greenhouse.

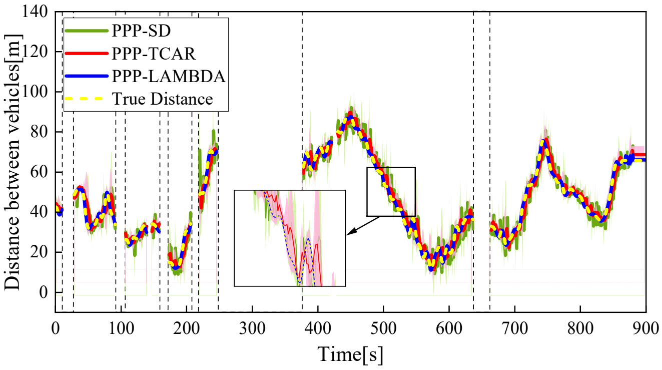

Figure 19. The distance between vehicles of RME in avenue.

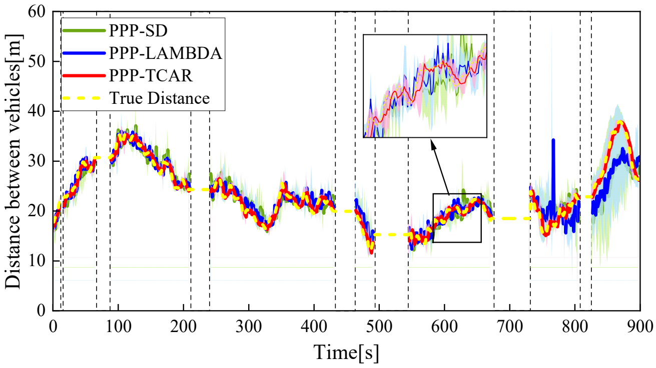

Figure 20. The distance between vehicles of RME in playground.

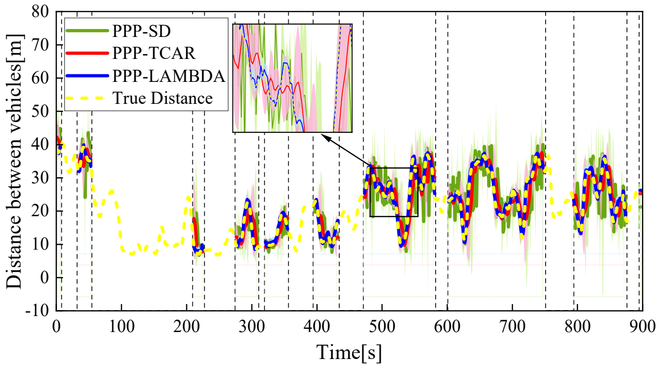

Figure 21. The distance between vehicles of RME in urban.

Through the above research, the framework constructed in this paper is integrated with different common field operation scenarios to evaluate the application level of the three algorithms and flexibly switch the positioning algorithm in different operation scenarios (Table 6).

Table 6. Multi-scenario variable-state fusion algorithm ranging analysis framework.

NO.	PPP-SD	PPP-TCAR	PPP-LAMBDA	Operation Status
Greenhouse farm machinery operation	*	**	***	Complete cover—absolute static state Complete cover—relative static state Complete cover—one moving and one static state Complete cover—random dynamic motion
Fixed-point picking operation of fruit forest	*	**	***	Partial cover—absolute static state Partial cover—relative static state Partial cover—one moving and one static state Partial cover—random dynamic motion
Cooperative operation of farm machinery in field	*	**	***	Open—absolute static state Open—relative static state
Farm machinery scheduling in the field	*	***	**	Open—one moving and one static state Open—random dynamic motion
Urban landscaping operations	*	**	***	“Urban Canyon” —absolute static state “Urban Canyon” —relative static state “Urban Canyon” —one moving and one static state “Urban Canyon” —random dynamic motion

Note: the symbol “*” means weak applicability, “**” means general applicability, and “***” means strong applicability.

4. Discussion

For the above experimental results, the principles of PPP-SD and PPP-DD (PPP-TCAR and PPP-LAMBDA) positioning are discussed and analyzed in conjunction with their positioning principles.

Pseudo-ranging positioning technology has been widely used. Study [20] established pseudo-ranging single-difference and double-difference ranging frameworks, and carried out positioning accuracy experiments in two different scenarios, and the results concluded that the positioning accuracy of double-difference is significantly better than that of single-difference positioning. This is because double-difference positioning is differential for two satellites based on single-difference positioning, and therefore can further eliminate the receiver clock difference in the measured values. The experimental results in this paper are the same as that study, with double-difference positioning accuracy outperforming single-difference positioning in different scenarios. However, adding one differential means increasing the complexity of the positioning system model. Therefore, it is necessary to investigate different double-difference positioning models. In the research results in Table 6, the PPP-LAMBDA algorithm has the strongest robustness and can adapt to the solution of multiple scenarios; PPP-TCAR uses a double-difference pseudo-range measurement to solve for the whole-week ambiguity of a double-difference carrier-phase measurement with a longer wavelength, thus obtaining an accurate distance measurement without ambiguity. The distance measurement just obtained is then used to solve for the perimeter ambiguity of another shorter wavelength double-difference carrier-phase measurement, and so on, step by step. As a result, PPP-TCAR is more dependent on valid satellite signals, and when the environment is favorable, PPP-TCAR exerts superior positioning performance [36].

However, some experimental results show (e.g., Figure 21) that when the environment is poor and affected by NLOS, the GNSS signal loses packets and some positioning data are missing. Therefore, to improve positioning accuracy and stability, multi-source information-assisted GNSS positioning will be one of the choices for intelligent farm equipment positioning. For example, GNSS/Ultra-wide Bandwidth (UWB) fusion positioning technology [38] is adopted to increase the UWB auxiliary base station as a pseudo-satellite to provide more ranging equations, and, at the same time, to make up for the shortcomings of the insufficient accuracy of indoor positioning of GNSS. Through the fusion of GNSS/UWB/Inertial Navigation System (INS) [39], it provides the motion attitude characteristics of the farm machinery body to solve the problem of packet loss in the case of NLOS of GNSS signals. Furthermore, the simultaneous localization and mapping (SLAM) technique [40], real-time dynamic acquisition of environmental features, is used to assist GNSS positioning. Inspired by this, in future research, the research of GNSS/UWB/INS/SLAM multi-source information fusion positioning technology based on the extended Kalman filter algorithm will be considered to improve the positioning accuracy of agricultural machines in different environments.

5. Conclusions

This paper proposes a multi-scenario variable-state fusion algorithm as a theoretical framework for observing the distance between vehicles. The performance of three different algorithms, PPP-SD, PPP-TCAR, and PPP-LAMBDA, was analyzed in four different scenarios with varying vehicle motion states. Specifically, this study focused on the impact of uncorrelated errors, such as the masking effect and multipath effect, on the accuracy of distance estimation. The experimental results indicate that the PPP-TCAR algorithm outperforms the others when the distance measurement is unaffected by these errors. However, in scenarios where complete cover, partial cover, and urban canyon effects are present, the PPP-LAMBDA algorithm demonstrated excellent accuracy, regardless of whether the vehicle was stationary or in motion. Therefore, when estimating distance in complex environments, it is recommended to use the PPP-LAMBDA algorithm, while the PPP-TCAR algorithm is optimal for open environments to achieve both accuracy and timeliness.

Author Contributions: Conceptualization, K.X. and Z.Z.; methodology, K.X.; software, K.X.; validation, F.W., Z.Z. and K.X.; formal analysis, K.X.; investigation, K.X.; resources, Z.Z.; data curation, K.X.; writing—original draft preparation, K.X.; writing—review and editing, F.W.; visualization, K.X.; supervision, Z.Z.; project administration, F.W.; funding acquisition, Z.Z. All authors have read and agreed to the published version of the manuscript.

Funding: This research was funded by the National Key Research and Development Program of China under grant 2022YFD2002004.

Data Availability Statement: The data presented in this study are available on request from the corresponding author.

Conflicts of Interest: The authors declare no conflicts of interest.

References

1. Radočaj, D.; Plaščak, I.; Jurišić, M. Global Navigation Satellite Systems as State-of-the-Art Solutions in Precision Agriculture: A Review of Studies Indexed in the Web of Science. *Agriculture* **2023**, *13*, 1417. [CrossRef]
2. Guo, W. Application of Geographic Information System and Automated Guidance System in Optimizing Contour and Terrace Farming. *Agriculture* **2018**, *8*, 142. [CrossRef]
3. Marucci, A.; Colantoni, A.; Zambon, I.; Egidi, G. Precision Farming in Hilly Areas: The Use of Network RTK in GNSS Technology. *Agriculture* **2017**, *7*, 60. [CrossRef]
4. Sambo, D.W.; Forster, A.; Yenke, B.O.; Sarr, I.; Gueye, B.; Dayang, P. Wireless Underground Sensor Networks Path Loss Model for Precision Agriculture (WUSN-PLM). *IEEE Sens. J.* **2020**, *20*, 5298–5312. [CrossRef]
5. Liu, Y.; Zhao, S.J.; Han, F.X.; Chai, M.Q.; Jiang, H.; Zhang, H.M. Data Collection for Target Localization in Ocean Monitoring Radar-Communication Networks. *Remote Sens.* **2023**, *15*, 5126. [CrossRef]
6. Chen, L.B.; Huang, G.Z.; Huang, X.R.; Wang, W.C. A Self-Supervised Learning-Based Intelligent Greenhouse Orchid Growth Inspection System for Precision Agriculture. *IEEE Sens. J.* **2022**, *22*, 24567–24577. [CrossRef]
7. Kan, X.Y.; Thayer, T.C.; Carpin, S.; Karydis, K. Task Planning on Stochastic Aisle Graphs for Precision Agriculture. *IEEE Robot. Autom. Lett.* **2021**, *6*, 3287–3294. [CrossRef]
8. Xue, D.Z.; Huang, W. Smart Agriculture Wireless Sensor Routing Protocol and Node Location Algorithm Based on Internet of Things Technology. *IEEE Sens. J.* **2021**, *21*, 24967–24973. [CrossRef]

9. Liu, Y.; Ma, X.Y.; Shu, L.; Hancke, G.P.; Abu-Mahfouz, A.M. From Industry 4.0 to Agriculture 4.0: Current Status, Enabling Technologies, and Research Challenges. *IEEE Trans. Ind. Inform.* **2021**, *17*, 4322–4334. [CrossRef]
10. Ding, F.; Zhang, W.; Luo, X.; Zhang, Z.; Wang, M.; Li, H.; Peng, M.; Hu, L. Design and Experiment for Inter-Vehicle Communication Based on Dead-Reckoning and Delay Compensation in a Cooperative Harvester and Transport System. *Agriculture* **2022**, *12*, 2052. [CrossRef]
11. Yang, L.; Wang, X.; Li, Y.; Xie, Z.; Xu, Y.; Han, R.; Wu, C. Identifying Working Trajectories of the Wheat Harvester In-Field Based on K-Means Algorithm. *Agriculture* **2022**, *12*, 1837. [CrossRef]
12. Sirikun, C.; Samseemoung, G.; Soni, P.; Langkapin, J.; Srinonchat, J. A Grain Yield Sensor for Yield Mapping with Local Rice Combine Harvester. *Agriculture* **2021**, *11*, 897. [CrossRef]
13. Rohani, M.; Gingras, D.; Vigneron, V.; Gruyer, D. A New Decentralized Bayesian Approach for Cooperative Vehicle Localization Based on Fusion of GPS and VANET Based Inter-Vehicle Distance Measurements. *IEEE Intell. Transp. Syst. Mag.* **2015**, *7*, 85–95. [CrossRef]
14. Naseri, H.; Koivunen, V. A Bayesian Algorithm for Distributed Network Localization Using Distance and Direction Data. *IEEE Trans. Signal Inf. Process Over Netw.* **2019**, *5*, 290–304. [CrossRef]
15. Wu, H.F.; Mei, X.J.; Chen, X.Q.; Li, J.J.; Wang, J.P. Mohapatra. A novel cooperative localization algorithm using enhanced particle filter technique in maritime search and rescue wireless sensor network. *ISA Trans.* **2018**, *78*, 39–46. [CrossRef] [PubMed]
16. Zhao, S.H.; Zhang, X.P.; Cui, X.W.; Lu, M.Q. Optimal Localization with Sequential Pseudorange Measurements for Moving Users in a Time Division Broadcast Positioning System. *IEEE Internet Things J.* **2021**, *8*, 8883–8896. [CrossRef]
17. Jiao, H.; Tao, X.; Chen, L.; Zhou, X.; Ju, Z. GNSS/5G Joint Position Based on Weighted Robust Iterative Kalman Filter. *Remote Sens.* **2024**, *16*, 1009. [CrossRef]
18. Nijak, M.; Skrzypczyński, P.; Ćwian, K.; Zawada, M.; Szymczyk, S.; Wojciechowski, J. On the Importance of Precise Positioning in Robotised Agriculture. *Remote Sens.* **2024**, *16*, 985. [CrossRef]
19. Ma, X.F.; Maruyama, T.; Ma, G.; Takeda, T. Determination of GPS receiver differential biases by neural network parameter estimation method. *Radio Sci.* **2005**, *40*, 1–13. [CrossRef]
20. Tahir, M.; Afzal, S.S.; Chughtai, M.S.; Ali, K. On the Accuracy of Inter-Vehicular Range Measurements Using GNSS Observables in a Cooperative Framework. *IEEE Trans. Intell. Transp. Syst.* **2019**, *20*, 682–691. [CrossRef]
21. Yan, Z.; Chen, X.Y.; Tang, X.H.; Zhu, X.F. Design and Performance Evaluation of the Improved INS-Assisted Vector Tracking for the Multipath in Urban Canyons. *IEEE Trans. Instrum. Meas.* **2022**, *71*, 1–16. [CrossRef]
22. Zhang, G.H.; Wen, W.S.; Xu, B.; Hsu, L.T. Extending Shadow Matching to Tightly-Coupled GNSS/INS Integration System. *IEEE Trans. Veh. Technol.* **2020**, *69*, 4979–4991. [CrossRef]
23. Yuan, Y.; Shen, F.; Li, X.D. GPS multipath and NLOS mitigation for relative positioning in urban environments. *Aerosp. Sci. Technol.* **2022**, *107*, 106315. [CrossRef]
24. Liu, K.; Lim, H.B.; Frazzoli, E.; Ji, H.L.; Lee, V.C.S. Improving Positioning Accuracy Using GPS Pseudorange Measurements for Cooperative Vehicular Localization. *IEEE Trans. Veh. Technol.* **2014**, *63*, 2544–2556. [CrossRef]
25. Shi, G.Q.; He, X.F.; Xiao, R.Y. Acquiring Three-Dimensional Deformation of Kilauea's South Flank from GPS and DInSAR Integration Based on the Ant Colony Optimization. *IEEE Geosci. Remote Sens. Lett.* **2015**, *12*, 2506–2510.
26. Zhang, Q.Q.; Zhao, L.; Zhou, J.H. A Novel Weighting Approach for Variance Component Estimation in GPS/BDS PPP. *IEEE Sens. J.* **2019**, *19*, 3763–3771. [CrossRef]
27. Jiang, W.; Li, Y.; Rizos, C. Optimal Data Fusion Algorithm for Navigation Using Triple Integration of PPP-GNSS, INS, and Terrestrial Ranging System. *IEEE Sens. J.* **2015**, *15*, 5634–5644. [CrossRef]
28. Li, T.; Pei, L.; Xiang, Y.; Wu, Q.; Xia, S.; Tao, L.H.; Guan, X.J.; Yu, W.X. P3-LOAM: PPP/LiDAR Loosely Coupled SLAM with Accurate Covariance Estimation and Robust RAIM in Urban Canyon Environment. *IEEE Sens. J.* **2021**, *21*, 6660–6671. [CrossRef]
29. Lee, H.K.; Lee, J.G.; Jee, G.I. GPS Multipath Detection Based on Sequence of Successive-Time Double-Differences. *IEEE Signal Process. Lett.* **2004**, *11*, 316–319. [CrossRef]
30. Scataglini, T.; Pagola, F.; Cogo, J.; Garca, J.G. Attitude Estimation Using GPS Carrier Phase Single Differences. *IEEE Lat. Am. Trans.* **2014**, *12*, 847–852. [CrossRef]
31. Bai, X.W.; Wen, W.S.; Hsu, L.T. Time-Correlated Window-Carrier-Phase-Aided GNSS Positioning Using Factor Graph Optimization for Urban Positioning. *IEEE Trans. Aerosp. Electron. Syst.* **2022**, *58*, 3370–3384. [CrossRef]
32. Pin, M.I.; Marucco, G.; Falco, G.; Gianluca, F.; Mario, N.; Wim, D.W. Experimental Testbed and Methodology for the Assessment of RTK GNSS Receivers Used in Precision Agriculture. *IEEE Access* **2020**, *8*, 14690–14703. [CrossRef]
33. Yang, X.; Shu, L.; Chen, J.N.; Ferrag, M.A.; Wu, J.; Nurellari, E.; Huang, K.A. Survey on Smart Agriculture: Development Modes, Technologies, and Security and Privacy Challenges. *IEEE/CAA J. Autom. Sin.* **2021**, *8*, 273–302. [CrossRef]
34. Yu, Y.; Chen, R.Z.; Shi, W.Z.; Chen, L. Precise 3D Indoor Localization and Trajectory Optimization Based on Sparse Wi-Fi FTM Anchors and Built-In Sensors. *IEEE Trans. Veh. Technol.* **2022**, *71*, 4042–4056. [CrossRef]
35. Hu, R.; Zhang, P.F.; Zhang, R.; Fan, L.H.; Han, J.Q.; Hong, J.; Liu, J.H.; Lu, X.C. Real-time and dynamic time transfer method based on double-differenced real-time kinematic mode. *IET Radar Sonar Navig.* **2021**, *15*, 143–153.
36. Li, B.F.; Feng, Y.M.; Shen, Y.Z. Three carrier ambiguity resolution: Distance-independent performance demonstrated using semi-generated triple frequency GPS signals. *GPS Solut.* **2010**, *14*, 177–184. [CrossRef]

37. Teunissen, P.J.G. The least-squares ambiguity decorrelation adjustment: A method for fast GPS integer ambiguity estimation. *J. Geod.* **1995**, *70*, 65–82. [CrossRef]
38. Zabalegui, P.; De Miguel, G.; Fernández-Berrueta, N.; Aizpuru, J.; Mendizabal, J.; Adín, I. On the Use of Ultra-WideBand-Based Augmentation for Precision Maneuvering. *Remote Sens.* **2024**, *16*, 911. [CrossRef]
39. Ren, Z.; Liu, S.; Liu, J.; Dai, J.; Lv, Y. Research on INS/GNSS/UWB Adaptive Robust ESKF Kinematic and Static Filtering Based on Cost Function. *Eng. Proc.* **2024**, *60*, 8.
40. Chen, Z.; Xu, A.; Sui, X.; Hao, Y.; Zhang, C.; Shi, Z. NLOS Identification- and Correction-Focused Fusion of UWB and LiDAR-SLAM Based on Factor Graph Optimization for High-Precision Positioning with Reduced Drift. *Remote Sens.* **2022**, *14*, 4258. [CrossRef]